To cite this version :

Mohamed BEN BETTAIEB, Farid ABED-MERAIM - Strain localization analysis for planar polycrystals based on bifurcation theory - Comptes Rendus Mécanique - Vol. 346, n°8, p.647-664 - 2018

To cite this version :

Mohamed BEN BETTAIEB, Farid ABED-MERAIM - Numerical investigation of localized necking of planar polycrystals - Comptes Rendus de Mécanique - Vol. 346, p.647-664 - 2018

Comptes Rendus Mecanique

Computational modeling of material forming processes / Simulation numérique des procédés de mise en forme

Strain localization analysis for planar polycrystals based on bifurcation theory

Mohamed Ben Bettaieb [a,b], Farid Abed-Meraim [a,b,*]

[a] *Arts et Métiers ParisTech, Université de Lorraine, CNRS, LEM3, 57000 Metz, France*
[b] *DAMAS, Laboratory of Excellence on Design of Alloy Metals for low-mAss Structures, Université de Lorraine, France*

abstract

In the present paper, an efficient numerical tool is developed to investigate the ductility limit of polycrystalline aggregates under in-plane biaxial loading. These aggregates are assumed to be representative of very thin sheet metals (with typically few grains through the thickness). Therefore, the plane-stress assumption is naturally adopted to numerically predict the occurrence of strain localization. Furthermore, the initial crystallographic texture is assumed to be planar. Considering the latter assumptions, a two-dimensional single-crystal model is advantageously chosen to describe the mechanical behavior at the microscopic scale. The mechanical behavior of the planar polycrystalline aggregate is derived from that of single crystals by using the full-constraint Taylor scale-transition scheme. To predict the occurrence of localized necking, the developed multiscale model is coupled with bifurcation theory. As will be demonstrated through various numerical results, in the case of biaxial loading under plane-stress conditions, the planar single-crystal model provides the same predictions as those given by the more commonly used three-dimensional single-crystal model. Moreover, the use of the two-dimensional model instead of the three-dimensional one allows dividing the number of active slip systems by two and, hence, significantly reducing the CPU time required for the integration of the constitutive equations at the single-crystal scale. Furthermore, the planar polycrystal model seems to be more suitable to study the ductility of very thin sheet metals, as its use allows us to rigorously ensure the plane-stress state, which is not always the case when the fully three-dimensional polycrystalline model is employed. Consequently, the adoption of this planar formulation, instead of the three-dimensional one, allows us to simplify the computational aspects and, accordingly, to considerably reduce the CPU time required for the numerical predictions.

1. Introduction

Over the last decades, the manufacture industry has been facing an increasing demand from customers for lightweight design to significantly reduce energy consumption and improve cost efficiency, while extending component service life by enhancing their ductility and mechanical resistance under a wide range of mechanical loading paths. Consequently, one of the main challenges in modern metal forming processes is to manufacture high-strength and light-weight structural components, which also greatly contribute to reducing carbon dioxide emissions. It is also well known that ductile failure is the main mechanism that limits material formability during forming processes. Ductile failure may be due to the accumulation of damage during the forming process or to the occurrence of localized necking without the presence of prior damage. The prediction of ductile failure during sheet metal forming processes using relevant damage models has been extensively studied in the literature. In this field, we can quote some phenomenological constitutive models developed to take into account the effect of the damage phenomenon on the evolution of plastic deformation through a scalar or tensor macroscopic damage variable (see, e.g., [1–3]). Damage description has been also considered in several multiscale schemes (such as the self-consistent scheme), where a damage variable has been introduced at a crystallographic slip system scale in order to better describe the material degradation by initiation, growth and coalescence of microdefects inside the polycrystalline material (see, e.g., [4,5]). In the present paper, we assume that ductile failure in traditional sheet metal forming processes (such as deep drawing and rolling) is solely due to the occurrence of localized necking (without the development of damage). To characterize the occurrence of localized necking and hence to predict the ductility limit of sheet metals, the classical concept of Forming Limit Diagram (FLD), initially introduced by Keeler and Backofen [6], has been widely used in both academia and industry. The numerical determination of FLDs requires the coupling between a strain localization criterion and a constitutive model, which describes the mechanical behavior of the studied material. Therefore, reliable predictions of localized necking cannot be achieved without resorting to efficient and accurate computational tools based on:

- the use of advanced constitutive modeling, which permits to accurately describe the mechanical behavior of the studied material and the influence of the key constitutive features on the initiation of localized necking. Indeed, it is widely recognized that the ductility limit is extremely sensitive to the mechanical and physical properties. Accordingly, a wide range of phenomenological behavior models has been implemented in several numerical tools to study the effect of some constitutive features on localized necking, such as plastic anisotropy [7,8], strain-rate sensitivity [9,10], and damage-induced softening [11,12]. Despite their good predictive capabilities and their wide use for the prediction of localized necking, the phenomenological models are not relevant enough to account for some key physical aspects of the material behavior, such as initial and induced textures and other microstructure-related parameters (dislocation motion and accumulation, grain morphology, crystallographic structures…). To address these limitations, micromechanical modeling has been recently used in several contributions to predict the ductility limit of metal sheets. Compared to phenomenological approaches, micromechanical descriptions reveal to be more appropriate to accurately link the above-mentioned microstructural parameters to the ductility limit. In this kind of modeling (namely micromechanical modeling), the constitutive equations are formulated at the single-crystal scale. Hence, these constitutive equations account for relevant mechanisms at this scale, such as lattice rotation, slip of crystallographic planes, hardening evolution, dislocation motion. The overall behavior of the polycrystalline aggregate is obtained from that of its single-crystal constituents by using some scale-transition schemes. Due to its good capabilities, the micromechanical modeling is largely followed in the literature to predict the ductility limit of thin metal sheets. The micromechanical models, mainly formulated within a finite strain framework, can be classified into two main families: rate-dependent and rate-independent frameworks; within the family of rate-dependent approaches, one can quote, for instance, Inal et al. [13], who have coupled the Taylor multiscale scheme with the initial imperfection approach developed by Marciniak and Kuczynski [14]. The same ductility limit approach has been coupled with the rate-dependent self-consistent scheme in several other works (see, e.g., [15,16]). As to the family of rate-independent approaches, fewer contributions have been developed, among which Knoackert et al. [17], who have coupled the initial imperfection approach with the Taylor multiscale model. More recently, the rate-independent self-consistent model has been coupled in [18,19] with Rice's bifurcation theory [20] to predict the incipience of plastic strain localization. Predictions of localized necking obtained by the initial imperfection approach have been compared to those given by bifurcation theory for the case of rate-independent materials in [18,21]. In [22], a homogenization-based finite element method has been coupled with the initial imperfection approach to analyze the occurrence of plastic flow localization in heterogeneous rate-independent materials. In the present investigation, our attention is confined to the ductility analysis of materials with FCC crystallographic structure. The mechanical behavior at the single-crystal scale is assumed to follow a large strain rate-independent framework. The plastic flow, which is assumed to be solely due to shear over crystallographic slip systems, is modeled by using the Schmid rule [23]. The evolution of the critical shear stresses, which is closely related to the evolution of the microscopic yield surfaces, is expressed through an isotropic hardening law. The rate-independent constitutive model chosen to describe the mechanical behavior at the single-crystal scale is known to be very accurate in the description of the deformation during cold-forming processes. Furthermore, it has been shown to be the most adequate framework for the prediction of localized necking based on bifurcation theory [18,19]. To derive the mechanical behavior of the polycrystalline aggregate from that of its single-crystal constituents, the full-constraint Taylor model is used in this work. Despite its simplicity, this multiscale scheme is able to accurately predict the texture evolution [24] and the ductility limit [21];
- the development of robust numerical tools that can efficiently predict strain localization. Indeed, numerical predictions based on micromechanical modeling generally require substantial amounts of CPU time and memory space. This is due, among other factors, to the fact that, in most numerical contributions devoted to the prediction of FLDs for thin sheet metals using multiscale schemes [16,18,19,21], the adopted polycrystalline model is formulated within the

general three-dimensional framework (at the single-crystal scale and, hence, at the polycrystalline scale). However, the plane-stress condition is commonly used to predict the occurrence of plastic strain localization. This assumption is fully justified by the very small thickness of the studied sheets compared to the other characteristic dimensions [25]. Thus, to ensure full compatibility and to link the three-dimensional behavior model to the two-dimensional formulation of the localization criterion, a two-dimensional formulation of the polycrystalline model should be derived from the original three-dimensional one. The derivation of such a two-dimensional formulation from the original one generally requires the application of an iterative computational procedure to reach the plane-stress state [18–21]. The major drawback of using a three-dimensional formulation of the constitutive equations, embedded into this iterative procedure to ensure the macroscopic plane-stress assumption, is that it requires substantial amounts of CPU time and memory space. Typically, the numerical determination of FLD for a polycrystalline aggregate composed of about 1000 grains needs many computation hours. Of course, this computation time depends on a number of mechanical choices (total number of slip systems for each single crystal, scale-transition scheme…), and numerical parameters (the selected increment for the strain–path ratio, the size of the strain step used to integrate the constitutive equations…). This computation time also depends on the number and speed of the processors used and on the level of parallelization, etc. Furthermore, the application of the above-described iterative procedure to a three-dimensional model allows satisfying the plane-stress state at the macroscopic level only. Indeed, under a three-dimensional formulation, the microscopic stress component normal to the plane of the sheet is heterogeneously distributed over the polycrystalline aggregate and is not necessarily equal to zero for all single crystals (only the volume average of this microscopic stress component is equal to zero). This observation reveals some inconsistency with the true plane-stress condition, which should be fulfilled at each material point of the sheet. Consequently, the development of robust numerical tools that aim to ensure the plane-stress condition at both the microscopic and macroscopic scales and to considerably reduce the CPU time represents a very attractive and challenging objective. One of the solutions, which can be followed to reach this objective, consists in using a two-dimensional idealization of polycrystalline models in the prediction of plastic strain localization. In these idealized models, the constitutive equations at the single-crystal scale are initially expressed under a two-dimensional formulation (two-dimensional slip systems). Within this formulation, the microscopic and macroscopic plane-stress conditions are naturally ensured without the need for resorting to any iterative procedure. This class of models has been originally developed by Asaro and Rice [26] to analyze plastic strain localization in ductile FCC single crystals deforming by single planar slip (instead of twelve slip systems in the general three-dimensional case). In this latter work, the plastic flow is modeled as rate-insensitive, and strain localization is viewed as a bifurcation from a homogeneous deformation mode to one that is concentrated on a narrow 'shear band' [20]. The pioneering analysis of Asaro and Rice [26], restricted to single crystals with a single slip system, has been extended by Asaro [27] to single crystals undergoing two symmetric slip systems in tension. In the two above-mentioned works [26,27], the single-crystal constitutive models have been purposely overly simplified in order to allow a deep understanding of the bifurcation phenomenon through purely analytical treatment. For this reason, these planar models have been widely used to gain a greater physical insight into these complex plastic instability phenomena. In this context, the two-dimensional model resulting from the double-slip mechanism developed by Asaro [27] has been coupled by Iwakuma and Nemat-Nasser [28] with the Hill self-consistent approach to derive the overall behavior of two-dimensional FCC polycrystalline aggregates. In this latter contribution, the self-consistent model has been coupled with the bifurcation approach (see, e.g., [29]) to predict the onset of strain localization in polycrystalline materials. Besides the analysis of strain localization in single crystals and polycrystals, the planar double-slip crystal models have been widely used to describe the mechanical behavior of thin structures and to predict the evolution of crystallographic texture during various deformation processes [30–34]. The model developed by Asaro [27] has been extended to a more general two-dimensional crystal constitutive description (see, e.g., [35,36]). Note that, contrary to the Asaro model, the two-dimensional constitutive description developed in [35] and [36] provides exactly the same predictions as those given by the three-dimensional model, when the loading is plane (biaxial strain and plane-stress states) and applied in one of the symmetry planes of the single crystal. In this particular case, biaxial strain state and plane-stress state become compatible (a biaxial strain state induces a plane-stress state and vice versa). This two-dimensional single-crystal model has been coupled in [24] with the Taylor scale-transition scheme to predict the texture evolution of planar polycrystalline aggregates. A planar polycrystal model, similar to the one used in [24], is coupled in the current contribution with the bifurcation approach to predict the occurrence of strain localization. As will be demonstrated through various numerical simulations, the results obtained by using the planar single crystal formulation are exactly the same as those given by the general three-dimensional model. However, the FLDs predicted by the two-dimensional polycrystalline model are very slightly different from those determined by the more commonly used three-dimensional model. This slight difference is due to a slight deviation from the microscopic plane-stress condition, which is rigorously satisfied only in the case of the two-dimensional model. In terms of computational efficiency, the use of the two-dimensional model instead of the three-dimensional one allows considerably reducing the computational cost required for the prediction of localized necking in thin sheet metals. To the authors' best knowledge, this is the first time that this planar polycrystal model is used to predict forming limit diagrams for polycrystalline aggregates.

The remainder of the paper is organized as follows:

- the second section is devoted to the presentation of the constitutive equations corresponding to the two-dimensional polycrystal model. This section also includes the algorithmic aspects relating to the numerical integration of these constitutive equations;
- the theoretical framework and the numerical implementation of the bifurcation approach are presented in detail in Section 3;
- the fourth section is dedicated to the presentation of various numerical results to illustrate the suitability of the planar polycrystal model in the prediction of localized necking.

2. Planar polycrystal model

2.1. Constitutive equations

The classical formulation of finite elasto-plastic deformation has been extensively studied in several early works (see, for instance, references [37–39]). This formulation assumes the existence of an infinite number of intermediate configurations (also called elastically relaxed configurations), obtained from the current one by elastic unloading to a stress-free state. Under this assumption, the total deformation gradient $\mathbf{f}$ may be multiplicatively decomposed into elastic and plastic parts, denoted $\mathbf{f}^{\mathrm{e}}$ and $\mathbf{f}^{\mathrm{p}}$, respectively:

$$\mathbf{f} = \mathbf{f}^{\mathrm{e}} \cdot \mathbf{f}^{\mathrm{p}} \tag{1}$$

Tensor $\mathbf{f}^{\mathrm{e}}$ may itself be multiplicatively decomposed into a stretching tensor $\mathbf{v}^{\mathrm{e}}$ and a rotation tensor $\mathbf{r}^{\mathrm{e}}$:

$$\mathbf{f}^{\mathrm{e}} = \mathbf{v}^{\mathrm{e}} \cdot \mathbf{r}^{\mathrm{e}} \tag{2}$$

Rotation $\mathbf{r}^{\mathrm{e}}$ defines the orientation of the intermediate configuration coordinate system with respect to the coordinate system related to the deformed configuration (current configuration).

Due to its suitability to describe the mechanical behavior of metallic materials, an Eulerian formulation is adopted to express the constitutive equations. Combining Eqs. (1) with (2), the velocity gradient $\mathbf{g}$ can be decomposed as follows:

$$\mathbf{g} = \dot{\mathbf{f}} \cdot \mathbf{f}^{-1} = \dot{\mathbf{f}}^{\mathrm{e}} \cdot \mathbf{f}^{\mathrm{e}-1} + \mathbf{f}^{\mathrm{e}} \cdot \dot{\mathbf{f}}^{\mathrm{p}} \cdot \mathbf{f}^{\mathrm{p}-1} \cdot \mathbf{f}^{\mathrm{e}-1} = \dot{\mathbf{v}}^{\mathrm{e}} \cdot \mathbf{v}^{\mathrm{e}-1} + \mathbf{v}^{\mathrm{e}} \cdot \dot{\mathbf{r}}^{\mathrm{e}} \cdot \mathbf{r}^{\mathrm{e}\mathsf{T}} \cdot \mathbf{v}^{\mathrm{e}-1} + \mathbf{v}^{\mathrm{e}} \cdot \mathbf{r}^{\mathrm{e}} \cdot \dot{\mathbf{f}}^{\mathrm{p}} \cdot \mathbf{f}^{\mathrm{p}-1} \cdot \mathbf{r}^{\mathrm{e}\mathsf{T}} \cdot \mathbf{v}^{\mathrm{e}-1} \tag{3}$$

By considering that the elastic strain is very small compared to the plastic strain, we can approximate the stretching tensor $\mathbf{v}^{\mathrm{e}}$ by the second-order identity tensor:

$$\mathbf{v}^{\mathrm{e}} \approx \mathbf{I}_2 \tag{4}$$

Under this approximation, Eq. (3) of the velocity gradient $\mathbf{g}$ can be reduced to:

$$\mathbf{g} = \dot{\mathbf{v}}^{\mathrm{e}} + \dot{\mathbf{r}}^{\mathrm{e}} \cdot \mathbf{r}^{\mathrm{e}\mathsf{T}} + \mathbf{r}^{\mathrm{e}} \cdot \dot{\mathbf{f}}^{\mathrm{p}} \cdot \mathbf{f}^{\mathrm{p}-1} \cdot \mathbf{r}^{\mathrm{e}\mathsf{T}} \tag{5}$$

Tensor $\mathbf{g}$ can also be decomposed into its symmetric part $\mathbf{d}$ and skew-symmetric part $\mathbf{w}$:

$$\mathbf{g} = \mathbf{d} + \mathbf{w} \tag{6}$$

The total strain rate tensor $\mathbf{d}$ and the total spin tensor $\mathbf{w}$ are in turn decomposed as follows:

$$\begin{array}{lll} \mathbf{d} = \mathbf{d}^{\mathrm{e}} + \mathbf{d}^{\mathrm{p}}; & \mathbf{d}^{\mathrm{e}} = \dot{\mathbf{v}}^{\mathrm{e}}; & \mathbf{d}^{\mathrm{p}} = \mathbf{r}^{\mathrm{e}} \cdot \left(\dot{\mathbf{f}}^{\mathrm{p}} \cdot \mathbf{f}^{\mathrm{p}-1}\right)_{\mathrm{S}} \cdot \mathbf{r}^{\mathrm{e}\mathsf{T}} \\ \mathbf{w} = \mathbf{w}^{\mathrm{e}} + \mathbf{w}^{\mathrm{p}}; & \mathbf{w}^{\mathrm{e}} = \dot{\mathbf{r}}^{\mathrm{e}} \cdot \mathbf{r}^{\mathrm{e}\mathsf{T}}; & \mathbf{w}^{\mathrm{p}} = \mathbf{r}^{\mathrm{e}} \cdot \left(\dot{\mathbf{f}}^{\mathrm{p}} \cdot \mathbf{f}^{\mathrm{p}-1}\right)_{\mathrm{A}} \cdot \mathbf{r}^{\mathrm{e}\mathsf{T}} \end{array} \tag{7}$$

where $\bullet_{\mathrm{S}}$ (resp., $\bullet_{\mathrm{A}}$) denotes the symmetric (resp., skew-symmetric) part of tensor $\bullet$.

As stated before, attention is confined in this paper to the study of FCC single crystals. The mechanical behavior of these crystals is assumed to follow a finite-strain rate-independent formulation, where the plastic deformation is only due to the slip on the crystallographic slip systems. Under this assumption, the plastic part of the velocity gradient $\mathbf{r}^{\mathrm{e}} \cdot (\dot{\mathbf{f}}^{\mathrm{p}} \cdot \mathbf{f}^{\mathrm{p}-1}) \cdot \mathbf{r}^{\mathrm{e}\mathsf{T}}$ can be written under the following form (for the particular case of FCC single crystals, the number of crystallographic slip systems is equal to 12):

$$\mathbf{r}^{\mathrm{e}} \cdot \left(\dot{\mathbf{f}}^{\mathrm{p}} \cdot \mathbf{f}^{\mathrm{p}-1}\right) \cdot \mathbf{r}^{\mathrm{e}\mathsf{T}} = \sum_{\alpha=1}^{12} \dot{\gamma}^{\alpha} \vec{\mathbf{m}}^{\alpha} \otimes \vec{\mathbf{n}}^{\alpha} \tag{8}$$

where $\dot{\gamma}^{\alpha}$ is the algebraic value of the slip rate for system α, and vector $\vec{\mathbf{m}}^{\alpha}$ (resp. $\vec{\mathbf{n}}^{\alpha}$) represents the slip direction (resp. the normal to the slip plane) in the current configuration. The counterparts of vectors $\vec{\mathbf{m}}^{\alpha}$ and $\vec{\mathbf{n}}^{\alpha}$ in the intermediate configuration, which are denoted respectively by $\underline{\vec{\mathbf{m}}}^{\alpha}$ and $\underline{\vec{\mathbf{n}}}^{\alpha}$, are defined by the following relations:

$$\vec{\mathbf{m}}^{\alpha} = \mathbf{r}^{\mathrm{e}} \cdot \underline{\vec{\mathbf{m}}}^{\alpha}; \qquad \vec{\mathbf{n}}^{\alpha} = \underline{\vec{\mathbf{n}}}^{\alpha} \cdot \mathbf{r}^{\mathrm{e}\mathsf{T}} \tag{9}$$

Table 1
The numbering of the three-dimensional slip systems for FCC single crystals.

α	1	2	3	4	5	6	7	8	9	10	11	12
$\sqrt{3}\vec{\mathbf{n}}_0^\alpha$	$\langle 1\ 1\ 1\rangle$	$\langle 1\ 1\ 1\rangle$	$\langle 1\ 1\ 1\rangle$	$\langle 1\ 1\ -1\rangle$	$\langle 1\ 1\ -1\rangle$	$\langle 1\ 1\ -1\rangle$	$\langle 1\ -1\ 1\rangle$	$\langle 1\ -1\ 1\rangle$	$\langle 1\ -1\ 1\rangle$	$\langle -1\ 1\ 1\rangle$	$\langle -1\ 1\ 1\rangle$	$\langle -1\ 1\ 1\rangle$
$\sqrt{2}\vec{\mathbf{m}}_0^\alpha$	$[1\ -1\ 0]$	$[1\ 0\ -1]$	$[0\ 1\ -1]$	$[1\ 0\ 1]$	$[1\ -1\ 0]$	$[0\ 1\ 1]$	$[1\ 0\ -1]$	$[0\ 1\ 1]$	$[1\ 1\ 0]$	$[0\ 1\ -1]$	$[1\ 1\ 0]$	$[1\ 0\ 1]$

In the particular case of single crystals, the intermediate configuration is chosen such that the vectors $\underline{\vec{\mathbf{m}}}^\alpha$ and $\underline{\vec{\mathbf{n}}}^\alpha$ remain constant, equal respectively to $\vec{\mathbf{m}}_0^\alpha$ and $\vec{\mathbf{n}}_0^\alpha$, during the deformation. The numbering of vectors $\vec{\mathbf{m}}_0^\alpha$ and $\vec{\mathbf{n}}_0^\alpha$ for FCC single crystals is given in Table 1.

To satisfy the objectivity principle, the lattice co-rotational derivative $\boldsymbol{\sigma}^\nabla$ of the Cauchy stress tensor $\boldsymbol{\sigma}$ is introduced by the following relation:

$$\boldsymbol{\sigma}^\nabla = \dot{\boldsymbol{\sigma}} - \mathbf{w}^{\mathrm{e}} \cdot \boldsymbol{\sigma} + \boldsymbol{\sigma} \cdot \mathbf{w}^{\mathrm{e}} \tag{10}$$

where $\dot{\boldsymbol{\sigma}}$ is the time derivative of the Cauchy stress tensor $\boldsymbol{\sigma}$, and $\mathbf{w}^{\mathrm{e}}$ is the elastic spin tensor introduced in Eq. $(7)_4$. Note that the lattice co-rotational derivative introduced in Eq. (10) is based on the elastic part of the spin tensor $\mathbf{w}^{\mathrm{e}}$. It is used instead of the well-known Jaumann derivative based on the total spin tensor $\mathbf{w}$ because it allows accurately following the rotation of the crystallographic lattice [27,40]. Tensor $\boldsymbol{\sigma}^\nabla$ can be related to the elastic strain rate $\mathbf{d}^{\mathrm{e}}$ by the isotropic fourth-order elasticity tensor $\mathbf{l}^{\mathrm{e}}$:

$$\boldsymbol{\sigma}^\nabla = \mathbf{l}^{\mathrm{e}} : \mathbf{d}^{\mathrm{e}} \tag{11}$$

For simplicity, the elastic behavior is modeled by an isotropic law, despite crystals have cubic symmetry. This choice is motivated by the fact that the effect of the elastic behavior on the prediction of the ductility limit (which is the main objective of the current contribution) remains very small.

The plastic flow of the single crystal is defined by the Schmid law [23]. This law states that slip may occur on a slip system α only when its resolved shear stress τ^α reaches a critical value τ_c^α (critical shear stress):

$$\forall\alpha = 1, \ldots, 12: \quad \begin{cases} |\tau^\alpha| < \tau_{\mathrm{c}}^\alpha \Rightarrow \dot{\gamma}^\alpha = 0 \\ |\tau^\alpha| = \tau_{\mathrm{c}}^\alpha \Rightarrow |\dot{\gamma}^\alpha| \geq 0 \end{cases} \tag{12}$$

where the resolved shear stress τ^α, acting on a given slip system α, is defined as the projection of the Cauchy stress $\boldsymbol{\sigma}$ on the Schmid tensor $\mathbf{M}^\alpha$ $(= \vec{\mathbf{m}}^\alpha \otimes \vec{\mathbf{n}}^\alpha)$ corresponding to that slip system:

$$\forall\alpha = 1, \ldots, 12: \quad \tau^\alpha = \boldsymbol{\sigma} : \mathbf{M}^\alpha \tag{13}$$

and τ_{c}^α is the critical shear stress. The evolution of τ_{c}^α is defined as a function of γ^α by the following hardening law:

$$\forall\alpha = 1, \ldots, 12: \quad \dot{\tau}_{\mathrm{c}}^\alpha = \sum_{\beta=1}^{12} h^{\alpha\beta} |\dot{\gamma}^\beta| \tag{14}$$

where $\mathbf{h}$ is the hardening matrix.

Taking into account Eq. (9), the resolved shear stress τ^α defined by Eq. (13) can be expressed as follows:

$$\forall\alpha = 1, \ldots, 12: \quad \tau^\alpha = \boldsymbol{\sigma} : \mathbf{M}^\alpha = \underline{\boldsymbol{\sigma}} : \underline{\mathbf{M}}^\alpha = \underline{\boldsymbol{\sigma}} : \left(\vec{\mathbf{m}}_0^\alpha \otimes \vec{\mathbf{n}}_0^\alpha\right) \quad \text{where } \underline{\boldsymbol{\sigma}} = \mathbf{r}^{\mathrm{e}\mathsf{T}} \cdot \boldsymbol{\sigma} \cdot \mathbf{r}^{\mathrm{e}} \tag{15}$$

A single crystal is known to be a three-dimensional anisotropic material, which means that a biaxial strain state ($g_{13} = g_{23} = g_{31} = g_{32} = 0$) may induce a three-dimensional stress state ($\sigma_{13} \neq 0$, $\sigma_{23} \neq 0$, $\sigma_{33} \neq 0$), and vice versa. Nevertheless, if the single crystal is submitted to in-plane loading along one of its symmetry planes, then the biaxial strain state and the plane-stress state become compatible, resulting in a true two-dimensional crystal model. As the loading paths adopted in the FLD predictions are plane (biaxial strain and plane-stress states), the two-dimensional crystal model seems to be a relevant model to describe the mechanical behavior at the microscopic level. As discussed earlier by Chenaoui et al. [24], FCC single crystals have two families of symmetry planes: {100} and {110}. The loading is said to be plane if it is applied along one of these symmetry planes. The application of loading along one of these two families of symmetry planes allows us to define two different planar FCC single crystal models: the PFCC1 for the {100} family, and the PFCC2 for the {110} family.

In the current investigation, focus is restricted to the PFCC1 model, with loading applied along the {001} plane. The concept of the PFCC1 model will be briefly recalled in the following developments. More details on this concept are given in Refs. [24,35,36].

Table 2
The numbering of the plane slip systems for the PFCC1 single crystal.

Planar slip system	Three-dimensional slip systems	In-plane Schmid tensor
1	1 ↔ 5	$\mathbf{X}_0^1 = \frac{1}{\sqrt{6}}\begin{bmatrix} 1 & 1 \\ -1 & -1 \end{bmatrix}$
2	2 ↔ 4	$\mathbf{X}_0^2 = \frac{1}{\sqrt{6}}\begin{bmatrix} 1 & 1 \\ 0 & 0 \end{bmatrix}$
3	3 ↔ 6	$\mathbf{X}_0^3 = \frac{1}{\sqrt{6}}\begin{bmatrix} 0 & 0 \\ 1 & 1 \end{bmatrix}$
4	7 ↔ 12	$\mathbf{X}_0^4 = \frac{1}{\sqrt{6}}\begin{bmatrix} 1 & -1 \\ 0 & 0 \end{bmatrix}$
5	8 ↔ 10	$\mathbf{X}_0^5 = \frac{1}{\sqrt{6}}\begin{bmatrix} 0 & 0 \\ 1 & -1 \end{bmatrix}$
6	9 ↔ 11	$\mathbf{X}_0^6 = \frac{1}{\sqrt{6}}\begin{bmatrix} 1 & -1 \\ 1 & -1 \end{bmatrix}$

In the particular case of the PFCC1 model, the rotation $\mathbf{r}^{\mathrm{e}}$ of the intermediate configuration with respect to the current one can be reduced to the following form:

$$\mathbf{r}^{\mathrm{e}} = \begin{bmatrix} \cos(\varphi) & \sin(\varphi) & 0 \\ -\sin(\varphi) & \cos(\varphi) & 0 \\ 0 & 0 & 1 \end{bmatrix} \tag{16}$$

Under the plane-stress condition, and taking into account the form (16) of the rotation $\mathbf{r}^{\mathrm{e}}$, the Cauchy stress tensor $\underline{\boldsymbol{\sigma}}$ in the intermediate configuration can be expressed by the following generic form:

$$\underline{\boldsymbol{\sigma}} = \mathbf{r}^{\mathrm{e}\mathsf{T}} \cdot \boldsymbol{\sigma} \cdot \mathbf{r}^{\mathrm{e}} = \mathbf{r}^{\mathrm{e}\mathsf{T}} \cdot \begin{bmatrix} \sigma_{11} & \sigma_{12} & 0 \\ \sigma_{12} & \sigma_{22} & 0 \\ 0 & 0 & 0 \end{bmatrix} \cdot \mathbf{r}^{\mathrm{e}} = \begin{bmatrix} \underline{\sigma}_{11} & \underline{\sigma}_{12} & 0 \\ \underline{\sigma}_{12} & \underline{\sigma}_{22} & 0 \\ 0 & 0 & 0 \end{bmatrix} \tag{17}$$

Let us consider, for instance, the crystallographic slip systems 1 and 5 (see Table 1). The Schmid tensors corresponding to these two systems can be expressed in the frame of the intermediate configuration as follows:

$$\underline{\mathbf{M}}^1 = \vec{\mathbf{m}}_0^1 \otimes \vec{\mathbf{n}}_0^1 = \frac{1}{\sqrt{6}} \begin{bmatrix} 1 & 1 & 1 \\ -1 & -1 & -1 \\ 0 & 0 & 0 \end{bmatrix}; \qquad \underline{\mathbf{M}}^5 = \vec{\mathbf{m}}_0^5 \otimes \vec{\mathbf{n}}_0^5 = \frac{1}{\sqrt{6}} \begin{bmatrix} 1 & 1 & -1 \\ -1 & -1 & 1 \\ 0 & 0 & 0 \end{bmatrix} \tag{18}$$

By analyzing the Schmid tensors of Eq. (18), one can conclude that:

- the crystallographic slip systems 1 and 5 have exactly the same resolved shear stress under the plane-stress condition,

$$\left.\begin{aligned} \tau^1 &= \underline{\boldsymbol{\sigma}} : \underline{\mathbf{M}}^1 = \frac{\underline{\sigma}_{11} - \underline{\sigma}_{22}}{\sqrt{6}} \\ \tau^5 &= \underline{\boldsymbol{\sigma}} : \underline{\mathbf{M}}^5 = \frac{\underline{\sigma}_{11} - \underline{\sigma}_{22}}{\sqrt{6}} \end{aligned}\right\} \quad \Rightarrow \quad \tau^1 = \tau^5 \tag{19}$$

- the contributions of both slip systems to the biaxial strain state are the same;
- the contributions of both slip systems to the strain components in the third direction are opposite.

Based on the latter analysis, one can clearly confirm that the crystallographic systems 1 and 5 are symmetric and identically loaded. Consequently, $\dot{\gamma}^1$ is identically equal to $\dot{\gamma}^5$ during the loading. Then, the contribution of these two slip systems to the plastic deformation $\dot{\mathbf{f}}^{\mathrm{p}} \cdot \mathbf{f}^{\mathrm{p}-1}$ is:

$$\begin{gathered} \dot{\gamma}^1 \vec{\mathbf{m}}_0^1 \otimes \vec{\mathbf{n}}_0^1 + \dot{\gamma}^5 \vec{\mathbf{m}}_0^5 \otimes \vec{\mathbf{n}}_0^5 = \dot{\gamma}^1 \left(\vec{\mathbf{m}}_0^1 \otimes \vec{\mathbf{n}}_0^1 + \vec{\mathbf{m}}_0^5 \otimes \vec{\mathbf{n}}_0^5\right) = \dot{\gamma}^1 \sqrt{\frac{2}{3}} \begin{bmatrix} 1 & 1 & 0 \\ -1 & -1 & 0 \\ 0 & 0 & 0 \end{bmatrix} \triangleq \dot{\eta}^1 \mathbf{X}_0^1 \\ \text{where } \dot{\eta}^1 = 2\dot{\gamma}^1 \quad \text{and} \quad \mathbf{X}_0^1 = \frac{1}{\sqrt{6}} \begin{bmatrix} 1 & 1 \\ -1 & -1 \end{bmatrix} \end{gathered} \tag{20}$$

which is a plane strain state (the components 13, 23, 31, and 32 are equal to 0). The two systems 1 and 5 can then be degenerated in one single-plane pseudo-slip system defined by its in-plane Schmid tensor $\mathbf{X}_0^1$. The other slip systems may be analyzed in a similar way: 2↔4, 3 ↔ 6, 7 ↔ 12, 8 ↔ 10, and 9 ↔ 11. Therefore, the 12 three-dimensional slip systems are symmetrized into 6-plane slip systems (see Table 2).

For the sake of simplicity, all vector and tensor fields used in the remainder of the paper will be expressed in their in-plane form without changing the notations adopted until now. For instance, tensor $\boldsymbol{\sigma}$ will be defined as follows:

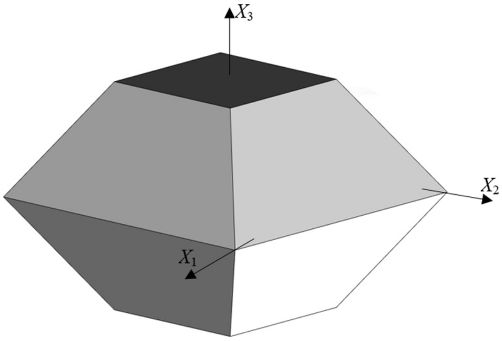

Fig. 1. Initial yield locus corresponding to the PFCC1 model in the (X_1, X_2, X_3) space.

$$\boldsymbol{\sigma} = \begin{bmatrix} \sigma_{11} & \sigma_{12} \\ \sigma_{12} & \sigma_{22} \end{bmatrix} \tag{21}$$

On the other hand, a tensor variable $\bullet$ will be denoted $\bullet_{3\mathcal{D}}$, when it is expressed in its three-dimensional form.

With these definitions and notations, Eq. (8) can be rewritten in its in-plane form:

$$\mathbf{r}^{\mathrm{e}} \cdot \left(\dot{\mathbf{f}}^{\mathrm{p}} \cdot \mathbf{f}^{\mathrm{p}-1}\right) \cdot \mathbf{r}^{\mathrm{e}\mathsf{T}} = \sum_{\alpha=1}^{6} \dot{\eta}^{\alpha} \mathbf{X}^{\alpha} \tag{22}$$

Similarly, the isotropic fourth-order elasticity tensor $\mathbf{l}^{\mathrm{e}}$, relating the elastic strain rate $\mathbf{d}^{\mathrm{e}}$ to the co-rotational derivative $\boldsymbol{\sigma}^{\nabla}$ of the stress tensor (see Eq. (11)), is defined by its matrix form (more adapted for the numerical implementation):

$$\mathbf{l}^{\mathrm{e}} = \frac{E}{1-\nu^2} \begin{bmatrix} 1 & \nu & 0 \\ \nu & 1 & 0 \\ 0 & 0 & \frac{1-\nu}{2} \end{bmatrix} \tag{23}$$

where E and ν are the Young modulus and the Poisson ratio.

As to the Schmid law given in Eq. (12), it is reformulated as follows:

$$\forall \alpha = 1, \ldots, 6: \quad \begin{cases} |\tau^{\alpha}| < \tau_{\mathrm{c}}^{\alpha} \Rightarrow \dot{\eta}^{\alpha} = 0 \\ |\tau^{\alpha}| = \tau_{\mathrm{c}}^{\alpha} \Rightarrow |\dot{\eta}^{\alpha}| \geq 0 \end{cases} \quad \text{where } \tau^{\alpha} = \boldsymbol{\sigma} : \mathbf{X}^{\alpha} \tag{24}$$

The initial yield locus corresponding to the PFCC1 model is a decahedron in the three-dimensional lattice–stress space, having the components X_1, X_2 and X_3 as axes, as shown in Fig. 1. The components X_1, X_2 and X_3 are determined by the following linear transformations from the components of tensor $\underline{\boldsymbol{\sigma}}$:

$$X_1 = \sqrt{2}\underline{\sigma}_{12}; \qquad X_2 = (\underline{\sigma}_{11} + \underline{\sigma}_{22})/\sqrt{2}; \qquad X_3 = (\underline{\sigma}_{11} - \underline{\sigma}_{22})/\sqrt{2} \tag{25}$$

For practical reasons related to the numerical implementation of the single-crystal constitutive equations, it is more suitable to only handle positive values of the slip rates. To this end, each slip system is split into two oriented slip systems. These oriented slip systems are characterized by the following Schmid tensors:

$$\mathbf{X}^{\alpha} = \begin{cases} \mathbf{X}^{\alpha} & \forall \alpha = 1, \ldots, 6 \\ -\mathbf{X}^{\alpha-6} & \forall \alpha = 7, \ldots, 12 \end{cases} \tag{26}$$

With the above conventions, which will be followed in the remainder of the paper, Eqs. (24), (14), and (22) become, respectively:

$$\begin{aligned} &\forall \alpha = 1, \ldots, 12: \quad \begin{cases} \tau^{\alpha} < \tau_{\mathrm{c}}^{\alpha} \Rightarrow \dot{\eta}^{\alpha} = 0 \\ \tau^{\alpha} = \tau_{\mathrm{c}}^{\alpha} \Rightarrow \dot{\eta}^{\alpha} \geq 0 \end{cases} \\ &\forall \alpha = 1, \ldots, 6: \quad \dot{\tau}_{\mathrm{c}}^{\alpha+6} = \dot{\tau}_{\mathrm{c}}^{\alpha} = \sum_{\beta=1}^{12} h^{\alpha\beta} \dot{\eta}^{\beta} \\ &\mathbf{r} \cdot \left(\dot{\mathbf{f}}^{\mathrm{p}} \cdot \mathbf{f}^{\mathrm{p}-1}\right) \cdot \mathbf{r}^{\mathsf{T}} = \sum_{\alpha=1}^{12} \dot{\eta}^{\alpha} \mathbf{X}^{\alpha} \end{aligned} \tag{27}$$

From Eq. $(27)_3$, the plastic strain rate $\mathbf{d}^{\mathrm{p}}$ and the plastic spin rate $\mathbf{w}^{\mathrm{p}}$ can be expressed as functions of tensors $\mathbf{R}^{\alpha}$ $(= (\mathbf{X}^{\alpha})_{\mathrm{S}})$ and $\mathbf{S}^{\alpha}$ $(= (\mathbf{X}^{\alpha})_{\mathrm{A}})$ as follows:

$$\mathbf{d}^{\mathrm{p}} = \sum_{\alpha=1}^{12} \dot{\eta}^{\alpha} \mathbf{R}^{\alpha}; \qquad \mathbf{w}^{\mathrm{p}} = \sum_{\alpha=1}^{12} \dot{\eta}^{\alpha} \mathbf{S}^{\alpha} \tag{28}$$

The combination of Eqs. (7)$_1$, (11), and (28)$_1$ leads to:

$$\boldsymbol{\sigma}^{\nabla} = \mathbf{l}^{\mathrm{e}} : \mathbf{d}^{\mathrm{e}} = \mathbf{l}^{\mathrm{e}} : \left(\mathbf{d} - \mathbf{d}^{\mathrm{p}}\right) = \mathbf{l}^{\mathrm{e}} : \left(\mathbf{d} - \sum_{\alpha=1}^{12} \dot{\eta}^{\alpha} \mathbf{R}^{\alpha}\right) \tag{29}$$

By introducing the set $\mathcal{A}$ of active slip systems ($\forall \alpha \in \mathcal{A} : \dot{\eta}^{\alpha} > 0$), and by taking into account Eq. (27)$_1$, one can easily demonstrate that the following condition is fulfilled:

$$\forall \alpha \in \mathcal{A}: \quad \dot{\chi} = \dot{\tau}^{\alpha} - \dot{\tau}_{\mathrm{c}}^{\alpha} = 0 \tag{30}$$

By using the definitions of τ^{α} and $\tau_{\mathrm{c}}^{\alpha}$, as well as the above developments, the following relation can be derived from Eq. (30):

$$\forall \alpha \in \mathcal{A}: \quad \mathbf{R}^{\alpha} : \mathbf{l}^{\mathrm{e}} : \mathbf{d} = \sum_{\beta \in \mathcal{A}} \left(h^{\alpha\beta} + \mathbf{R}^{\alpha} : \mathbf{l}^{\mathrm{e}} : \mathbf{R}^{\beta}\right) \dot{\eta}^{\beta} \tag{31}$$

Thus, the slip rates of the active slip systems read:

$$\forall \alpha \in \mathcal{A}: \quad \dot{\eta}^{\alpha} = \sum_{\beta \in \mathcal{A}} M^{\alpha\beta} \mathbf{R}^{\beta} : \mathbf{l}^{\mathrm{e}} : \mathbf{d} \tag{32}$$

where $\mathbf{M}$ is the inverse of matrix $\mathbf{B}$, defined by the following index form:

$$\forall \alpha, \beta \in \mathcal{A}: \quad B^{\alpha\beta} = h^{\alpha\beta} + \mathbf{R}^{\alpha} : \mathbf{l}^{\mathrm{e}} : \mathbf{R}^{\beta} \tag{33}$$

To apply the bifurcation criterion detailed in Section 3, let us introduce the microscopic tangent modulus $\mathbf{l}$, which relates the nominal stress rate tensor $\dot{\mathbf{n}}$ to the velocity gradient $\mathbf{g}$:

$$\dot{\mathbf{n}} = \mathbf{l} : \mathbf{g} \tag{34}$$

The expression of $\dot{\mathbf{n}}$ can be obtained from the definition of the three-dimensional nominal stress tensor $\mathbf{n}_{3\mathcal{D}}$, which is given as follows:

$$\mathbf{n}_{3\mathcal{D}} = j_{3\mathcal{D}} \mathbf{f}_{3\mathcal{D}}^{-1} . \boldsymbol{\sigma}_{3\mathcal{D}} \tag{35}$$

The time derivative of Eq. (35) gives:

$$\dot{\mathbf{n}}_{3\mathcal{D}} = j_{3\mathcal{D}} \mathbf{f}_{3\mathcal{D}}^{-1} . \left(\dot{\boldsymbol{\sigma}}_{3\mathcal{D}} + \boldsymbol{\sigma}_{3\mathcal{D}} \operatorname{Tr}(\mathbf{d}_{3\mathcal{D}}) - \mathbf{g}_{3\mathcal{D}} . \boldsymbol{\sigma}_{3\mathcal{D}}\right) \tag{36}$$

An updated Lagrangian formulation (i.e. $\mathbf{f}_{3\mathcal{D}} = \mathbf{1}_{3\mathcal{D}}$ and $j_{3\mathcal{D}} = 1$) is adopted in what follows. Within this formulation, Eq. (36) becomes:

$$\dot{\mathbf{n}}_{3\mathcal{D}} = \dot{\boldsymbol{\sigma}}_{3\mathcal{D}} + \boldsymbol{\sigma}_{3\mathcal{D}} \operatorname{Tr}(\mathbf{d}_{3\mathcal{D}}) - \mathbf{g}_{3\mathcal{D}} \cdot \boldsymbol{\sigma}_{3\mathcal{D}} \tag{37}$$

Making use of Eqs. (7), (8), (10), and (11), one can demonstrate, after some straightforward developments, that $\dot{\mathbf{n}}$ can be expressed as a function of the slip rates $\dot{\eta}^{\alpha}$ as follows:

$$\dot{\mathbf{n}} = \left(\mathbf{l}^{\mathrm{e}} + \chi \boldsymbol{\sigma} \otimes \mathbf{1}\right) : \mathbf{d} - \boldsymbol{\sigma} \cdot \mathbf{w} - \mathbf{d} \cdot \boldsymbol{\sigma} - \sum_{\alpha \in \mathcal{A}} \left(\mathbf{l}^{\mathrm{e}} : \mathbf{R}^{\alpha} + \mathbf{S}^{\alpha} \cdot \boldsymbol{\sigma} - \boldsymbol{\sigma} \cdot \mathbf{S}^{\alpha}\right) \dot{\eta}^{\alpha} \tag{38}$$

where χ is defined by the following equation:

$$\chi = \frac{\operatorname{Tr}(\mathbf{d}_{3\mathcal{D}})}{\operatorname{Tr}(\mathbf{d})} = \frac{E \operatorname{Tr}(\dot{\boldsymbol{\sigma}})}{(1 - 2\nu)(d_{11} + d_{22})} \tag{39}$$

Substituting the slip rates $\dot{\eta}^{\alpha}$ in Eq. (38) by their expression from Eq. (32), one obtains, after straightforward algebraic manipulations, the following relation:

$$\dot{\mathbf{n}} = \left[\left(\mathbf{l}^{\mathrm{e}} + \chi \boldsymbol{\sigma} \otimes \mathbf{1}\right) - {}^{1}_{\boldsymbol{\sigma}}\mathbf{l} - {}^{2}_{\boldsymbol{\sigma}}\mathbf{l} - \sum_{\alpha, \beta \in \mathcal{A}} \left(\mathbf{l}^{\mathrm{e}} : \mathbf{R}^{\alpha} + \mathbf{S}^{\alpha} \cdot \boldsymbol{\sigma} - \boldsymbol{\sigma} \cdot \mathbf{S}^{\alpha}\right) M^{\alpha\beta} \mathbf{R}^{\beta} : \mathbf{l}^{\mathrm{e}}\right] : \mathbf{g} \tag{40}$$

where ${}^{1}_{\boldsymbol{\sigma}}\mathbf{l}$ and ${}^{2}_{\boldsymbol{\sigma}}\mathbf{l}$ are forth-order tensors comprising convective terms of the Cauchy stress components. Their index forms are given by the following relations:

$$ {}^{1}_{\sigma}l_{\mathrm{ijkl}} = \frac{1}{2}(\delta_{jl}\sigma_{ik} - \delta_{jk}\sigma_{il}); \qquad {}^{2}_{\sigma}l_{\mathrm{ijkl}} = \frac{1}{2}(\delta_{ik}\sigma_{jl} + \delta_{il}\sigma_{jk}) \tag{41} $$

where δ_{jl} denotes the Kronecker delta. Finally, the analytical tangent modulus $\mathbf{l}$ relating the nominal stress rate $\dot{\mathbf{n}}$ to the velocity gradient $\mathbf{g}$ can be easily identified from Eq. (40):

$$ \mathbf{l} = \left(\mathbf{l}^{\mathrm{e}} + \chi\boldsymbol{\sigma}\otimes\mathbf{1}\right) - {}^{1}_{\sigma}\mathbf{l} - {}^{2}_{\sigma}\mathbf{l} - \sum_{\alpha,\beta\in\mathcal{A}} \left(\mathbf{l}^{\mathrm{e}} : \mathbf{R}^{\alpha} + \mathbf{S}^{\alpha}\cdot\boldsymbol{\sigma} - \boldsymbol{\sigma}\cdot\mathbf{S}^{\alpha}\right) M^{\alpha\beta}\mathbf{R}^{\beta} : \mathbf{l}^{\mathrm{e}} \tag{42} $$

All the above constitutive equations – from Eq. (1) to Eq. (42) – correspond to the microscopic level (the single crystal scale). To model the mechanical behavior of a polycrystalline aggregate (which is assumed to be representative of the studied metal sheet) from the modeling at the single-crystal scale, the Taylor multiscale scheme is used. This scheme assumes strain homogeneity at the polycrystalline scale and is used to compute the macroscopic tangent modulus $\mathbf{L}$. The latter relates the macroscopic nominal stress rate $\dot{\mathbf{N}}$ to the macroscopic velocity gradient $\mathbf{G}$:

$$ \dot{\mathbf{N}} = \mathbf{L} : \mathbf{G} \tag{43} $$

Considering the strain homogeneity assumption, one obtains:

$$ \mathbf{G} = \mathbf{g} \quad \text{and} \quad \mathbf{L} = \frac{1}{V}\int_{V} \mathbf{l}\,\mathrm{d}\mathbf{x} \tag{44} $$

where V is the current volume of the polycrystalline aggregate.

2.2. Numerical integration

The constitutive equations at the single-crystal scale are solved by using an incremental algorithm over a typical time increment $\mathrm{I}^{\Delta} = [t_0, t_0 + \Delta t]$. This algorithm belongs to the family of ultimate algorithms, initially introduced by Borja and Wren [41] for the case of linear constitutive equations (without material and geometric non-linearities). More recently, Ben Bettaieb et al. [42,43] have developed explicit and implicit versions of the ultimate algorithm to take into account the non-linear behavior (non-linear hardening, finite strain, and finite rotation). Due to its computational efficiency, the explicit ultimate algorithm developed by Akpama et al. [43] is used in this paper, after some significant improvements. In the latter reference, it has been demonstrated that the ultimate algorithm is much more efficient and more robust than the return-mapping algorithm introduced by Anand and Kothari [44] in the case of rate-independent single-crystal constitutive equations. This ultimate algorithm is based on the idea of partition of the time increment I^{Δ} into several sub-increments $\mathrm{I}^{\delta_n} = [t_n, t_{n+1}]$ (where $t_{n=0} = t_0$). The size of sub-increments $\delta t_n = t_{n+1} - t_n$ and their number are a priori unknown. The size δt_n is determined in such a way that the Schmid criterion $(27)_1$ remains fulfilled over I^{δ_n}. By adopting this partition, the constitutive equations at the single-crystal scale must be integrated over each time sub-increment I^{δ_n}, where the known quantities are: the material parameters (elasticity and hardening), the mechanical fields $\boldsymbol{\sigma}$, $\mathbf{r}^{\mathrm{e}}$, and $\tau_{\mathrm{c}}^{\alpha}$ (for $\alpha = 1, \ldots, 6$) at t_n, and the velocity gradient $\mathbf{g}$ assumed to be constant over I^{Δ} (hence, over I^{δ_n}). The aim of the incremental algorithm is to compute the values of $\boldsymbol{\sigma}$, $\mathbf{r}^{\mathrm{e}}$, $\tau_{\mathrm{c}}^{\alpha}$ and $\mathbf{l}$ at t_{n+1}. By analyzing the single-crystal constitutive equations, it is clear that the determination of the slip rates $\dot{\eta}^{\alpha}$ for the different slip systems allows the computation of the other mechanical variables over the current time sub-increment I^{δ_n}. To compute $\dot{\eta}^{\alpha}$ for all slip systems, let us introduce the set of potentially active slip systems $\mathcal{P}$ at t_n:

$$ \mathcal{P} = \left\{\alpha = 1, \ldots, 12;\ \tau^{\alpha}(t_n) - \tau_{\mathrm{c}}^{\alpha}(t_n) = \boldsymbol{\sigma}(t_n) : \mathbf{R}^{\alpha}(t_n) - \tau_{\mathrm{c}}^{\alpha}(t_n) = 0\right\} \tag{45} $$

Considering Eq. (45), the Schmid law given by Eq. $(27)_1$, reduced to the potentially active slip system, can be rewritten as follows:

$$ \forall\alpha\in\mathcal{P}: \quad \dot{\chi}^{\alpha}(t_n) = \dot{\tau}_{\mathrm{c}}^{\alpha}(t_n) - \dot{\tau}^{\alpha}(t_n) \geq 0; \qquad \dot{\eta}^{\alpha}(t_n) \geq 0; \qquad \dot{\chi}^{\alpha}(t_n)\dot{\eta}^{\alpha}(t_n) = 0 \tag{46} $$

Eq. (46) may be viewed as a non-smooth complementarity problem and can therefore be replaced by an equivalent mathematical system involving the semi-smooth Fischer–Burmeister function [45,46]:

$$ \forall\alpha\in\mathcal{P}: \quad \xi^{\alpha}(t_n) = \sqrt{\left(\dot{\chi}^{\alpha}(t_n)\right)^2 + \left(\dot{\eta}^{\alpha}(t_n)\right)^2} - \left(\dot{\chi}^{\alpha}(t_n) + \dot{\eta}^{\alpha}(t_n)\right) = 0 \tag{47} $$

which can be efficiently solved by using the iterative Newton–Raphson method, where the main unknowns are the slip rates $\dot{\eta}^{\alpha}$ of the potentially active slip systems. To apply this Newton–Raphson method, a Jacobian matrix $\mathcal{J}$ should be computed at each iteration. This matrix is defined by the following index form:

$$ \forall\alpha,\beta\in\mathcal{P}: \quad \mathcal{J}^{\alpha\beta}(t_n) = \frac{\partial\xi^{\alpha}(t_n)}{\partial\dot{\eta}^{\beta}(t_n)} \tag{48} $$

The pseudo-inversion technique (see [44]) is used to invert the Jacobian matrix $\mathcal{J}$ when it is singular. The Newton–Raphson iterations are carried out until reaching the following convergence criterion:

$$\left\|\xi^{\alpha}(t_n)\right\| < 10^{-5} \tag{49}$$

It must be noted that, during the global Newton–Raphson iterations, no ad hoc assumptions are necessary concerning the determination of the active set of slip systems. Indeed, the use of the semi-smooth function (47), instead of the initial formulation (46), permits to combine both tasks, namely the identification of the set of active slip systems and the computation of the corresponding slip rates. This combination allows us to significantly increase the efficiency of the developed numerical scheme.

Once the slip rates of the potentially active slip systems are computed, the length δt_n of the sub-increment I^{δ_n} can be determined. δt_n should be inferior or equal to Δt and it is determined in such a way that the Schmid criterion remains satisfied for all slip systems. In view of Eq. (46), it is obvious that this criterion is fulfilled for the potentially active slip systems. For the other systems ($\notin \mathcal{P}$), the following condition must be verified:

$$\forall \alpha \notin \mathcal{P}: \quad \tau^{\alpha}(t_n + \delta t_n) \leq \tau_{\mathrm{c}}^{\alpha}(t_n + \delta t_n) \tag{50}$$

By using the definitions of τ^{α} and $\tau_{\mathrm{c}}^{\alpha}$, the following relations can be easily obtained:

$$\forall \alpha \notin \mathcal{P}: \quad \begin{cases} \tau^{\alpha}(t_n + \delta t_n) = \tau^{\alpha}(t_n) + \delta t_n \mathbf{R}^{\alpha}(t_n) : \boldsymbol{\sigma}^{\nabla}(t_n) \\ \qquad\qquad\quad\;\; = \tau^{\alpha}(t_n) + \delta t_n \mathbf{R}^{\alpha}(t_n) : \mathbf{l}^{\mathrm{e}} : (\mathbf{d} - \dot{\eta}^{\alpha}(t_n)\mathbf{R}^{\alpha}(t_n)) \\ \tau_{\mathrm{c}}^{\alpha}(t_n + \delta t_n) = \tau_{\mathrm{c}}^{\alpha}(t_n) + \delta t_n \sum_{\beta \in \mathcal{P}} h^{\alpha\beta}(t_n)\dot{\eta}^{\beta}(t_n) \end{cases} \tag{51}$$

The combination of Eqs. (50) and (51) provides the following condition on δt_n:

$$\delta t_n = \min_{\alpha \notin \mathcal{P}} \left\{ \Delta t, \frac{\tau_{\mathrm{c}}^{\alpha}(t_n) - \tau^{\alpha}(t_n)}{\mathbf{R}^{\alpha}(t_n) : \mathbf{l}^{\mathrm{e}} : (d - \dot{\eta}^{\alpha}(t_n)\mathbf{R}^{\alpha}(t_n)) - \sum_{\beta \in \mathcal{P}} h^{\alpha\beta}(t_n)\dot{\eta}^{\beta}(t_n)} \right\} \tag{52}$$

Once the length δt_n is determined, the other mechanical variables are updated as follows:

$$\begin{aligned} &\delta\mathbf{r} = \mathbf{exp}\left(\delta t_n \left(\mathbf{w} - \sum_{\alpha \in \mathcal{P}} \dot{\eta}^{\alpha}(t_n)\mathbf{S}^{\alpha}(t_n)\right)\right) \\ &\mathbf{r}^{\mathrm{e}}(t_n + \delta t_n) = \delta\mathbf{r}^{\mathrm{e}} \cdot \mathbf{r}^{\mathrm{e}}(t_n) \\ &\boldsymbol{\sigma}(t_n + \delta t_n) = \delta\mathbf{r}^{\mathrm{e}} \cdot \left[\boldsymbol{\sigma}(t_n) + \delta t_n \mathbf{l}^{\mathrm{e}} : \left(\mathbf{d} - \sum_{\alpha \in \mathcal{P}} \dot{\eta}^{\alpha}(t_n)\mathbf{R}^{\alpha}(t_n)\right)\right] \cdot \delta\mathbf{r}^{\mathrm{e}\mathsf{T}} \\ &\forall \alpha = 1, \ldots, 12: \quad \begin{cases} \tau_{\mathrm{c}}^{\alpha}(t_n + \delta t_n) = \tau_{\mathrm{c}}^{\alpha}(t_n) + \delta t_n \sum_{\beta \in \mathcal{P}} h^{\alpha\beta}(t_n)\dot{\eta}^{\beta}(t_n) \\ \mathbf{R}^{\alpha}(t_n + \delta t_n) = \mathbf{r}^{\mathrm{e}}(t_n + \delta t_n) \cdot \left(\mathbf{X}_0^{\alpha}\right)_{\mathrm{S}} \cdot \mathbf{r}^{\mathrm{e}\mathsf{T}}(t_n + \delta t_n) \\ \mathbf{S}^{\alpha}(t_n + \delta t_n) = \mathbf{r}^{\mathrm{e}}(t_n + \delta t_n) \cdot \left(\mathbf{X}_0^{\alpha}\right)_{\mathrm{A}} \cdot \mathbf{r}^{\mathrm{e}\mathsf{T}}(t_n + \delta t_n) \end{cases} \end{aligned} \tag{53}$$

The size of the time increment Δt and the initial time t_n are also updated:

$$\Delta t \leftarrow \Delta t - \delta t_n; \qquad t_n \leftarrow t_n + \delta t_n \tag{54}$$

After this update procedure, the computation should be restarted with a new sub-increment I^{δ_n}, until reaching the following condition:

$$\Delta t = \delta t_n \tag{55}$$

Once the different mechanical variables are updated by using Eq. (53), the microscopic tangent modulus $\mathbf{l}(t_0 + \Delta t)$ at the end of the time increment I^{Δ} must be computed. The macroscopic tangent modulus $\mathbf{L}(t_0 + \Delta t)$ is then derived by using the averaging relation $(44)_2$.

3. Bifurcation theory

Bifurcation theory (see, e.g., [20,29]) is used here to predict the occurrence of localized necking in polycrystalline aggregates. This theoretical approach assumes that the aggregate undergoes a homogeneous strain state before the onset of strain localization. Therefore, in such an approach, diffuse necking, which usually occurs prior to localized necking, is implicitly excluded. Furthermore, the thickness of the studied sheets is assumed to be very small compared to the other characteristic dimensions. With these modeling choices, it can be legitimately assumed that the strain homogeneity and plane-stress conditions are satisfied until the onset of localized necking. The governing equations and the algorithmic aspects corresponding to bifurcation theory are detailed in Sections 3.1 and 3.2, respectively.

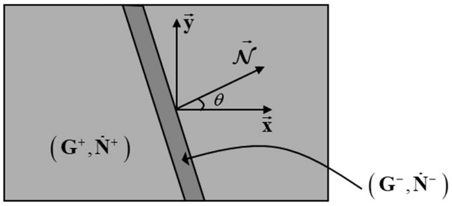

Fig. 2. Localization of the deformation along a narrow band.

3.1. *Governing equations*

In the approach proposed by Rice and co-workers [15,16,19], material instability corresponds to a bifurcation associated with admissible jumps for strain and stress rates across a localization band, as illustrated in Fig. 2. Since field equations have to be satisfied, the kinematic condition for the strain rate jump writes:

$$[\![\mathbf{G}]\!] = \mathbf{G}^+ - \mathbf{G}^- = \dot{\vec{\mathbf{C}}} \otimes \vec{\mathcal{N}} \tag{56}$$

where:

- $[\![\mathbf{G}]\!]$ is the jump of the field $\mathbf{G}$ across the discontinuity band;
- $\dot{\vec{\mathbf{C}}}$ is the jump vector;
- $\vec{\mathcal{N}}$ is the unit vector normal to the localization band.

On the other hand, the continuity of the equilibrium of forces through the band is expressed as:

$$\vec{\mathcal{N}} \cdot [\![\dot{\mathbf{N}}]\!] = \vec{\mathbf{0}} \tag{57}$$

The combination of Eqs. (56) and (57) with the constitutive law (43) leads to the following equation:

$$\vec{\mathcal{N}} \cdot (\mathbf{L} : \dot{\vec{\mathbf{C}}} \otimes \vec{\mathcal{N}}) = \vec{\mathbf{0}} \tag{58}$$

which is equivalent to:

$$(\vec{\mathcal{N}} \cdot \mathbf{L} \cdot \vec{\mathcal{N}}) \cdot \dot{\vec{\mathbf{C}}} = \vec{\mathbf{0}} \tag{59}$$

where $\vec{\mathcal{N}} \cdot \mathbf{L} \cdot \vec{\mathcal{N}}$ is the so-called acoustic tensor. As long as this tensor is invertible, the jump vector $\dot{\vec{\mathbf{C}}}$ remains equal to zero, thus precluding any discontinuity (bifurcation) in the deformation field. However, when the acoustic tensor becomes singular, there are non-zero jump vectors that satisfy Eq. (59), and this can be seen as an indicator of effective bifurcation. From a numerical point of view, strain localization occurs when the acoustic tensor is no longer invertible:

$$\det(\vec{\mathcal{N}} \cdot \mathbf{L} \cdot \vec{\mathcal{N}}) = \vec{0} \tag{60}$$

Eq. (60) is the so-called Rice bifurcation criterion, which corresponds to the loss of ellipticity of the partial differential equations governing the associated boundary value problem.

3.2. *Algorithmic aspects*

To determine FLDs, proportional strain paths are applied to the polycrystalline aggregate, which are characterized by constant strain–path ratios ρ. The two-dimensional macroscopic velocity gradient corresponding to these strain paths is defined by the following generic expression:

$$\mathbf{G} = \begin{pmatrix} G_{11} & 0 \\ 0 & \rho G_{11} \end{pmatrix} \tag{61}$$

Our main objective through the current contribution is not to predict forming limit diagrams and to analyze the corresponding numerical results (readers interested in this matter may consult Refs. [18,19]). Instead, we are particularly interested in establishing a comparative study between the two polycrystalline models (two-dimensional and three-dimensional) when they are applied to the prediction of localized necking. Accordingly, to reduce the computational costs, our numerical predictions are restricted to the negative range of strain paths ($-1/2 \le \rho \le 0$). In this range, the initial crystallographic texture has a strong effect on the behavior of the polycrystalline aggregate, which can be considered as a real heterogeneous medium.

The general algorithm for the FLD prediction based on the bifurcation approach relies on two nested loops:

- for each strain–path ratio ρ varying from $-1/2$ (uniaxial tensile state) to 0 (plane strain state), with $\Delta\rho = 0.1$:
  - for each time step $\mathrm{I}^{\Delta} = [t_0, t_0 + \Delta t]$, apply the algorithm developed in Section 2.2 to integrate the constitutive equations of the polycrystal corresponding to the safe zone (i.e. outside the localization band). With this aim, the two-dimensional macroscopic velocity gradient $\mathbf{G}$ given by Eq. (61) is used as loading, with the component G_{11} fixed to 1. After applying this algorithm, the macroscopic tangent modulus $\mathbf{L}$ must be determined at $t_0 + \Delta t$. The determinant of the acoustic tensor $\vec{\mathcal{N}} \cdot \mathbf{L} \cdot \vec{\mathcal{N}}$ is minimized over all band orientations θ ranging from 0° to 90°. If the computed minimum is inferior or equal to zero, then localized necking is detected. The corresponding angle θ is the orientation of the localization band, while the corresponding principal logarithmic strain is the predicted limit strain E_{11}. The computation is then stopped. Otherwise, the integration is continued for the next time increment I^{Δ}.

It must be noted that the same algorithm can be used to predict bifurcation with a three-dimensional model, after some small modifications. Indeed, a third nested loop should be embedded within the second loop (corresponding to the time integration over each time increment). This third loop aims to ensure the macroscopic plane-stress condition:

$$\dot{\Sigma}_{3\mathcal{D}33} = 0 \quad \Leftrightarrow \quad \dot{\mathbf{N}}_{3\mathcal{D}33} = 0 \tag{62}$$

In this latter three-dimensional case, the macroscopic velocity gradient $G_{3\mathcal{D}33}$ is a priori unknown, and it is iteratively computed on the basis of the fixed point method to fulfill condition (62). After careful checking (based on various polycrystalline simulations), we can confirm that the convergence of this iterative scheme is always ensured (provided that the time step remains relatively small), leading to a unique solution to the macroscopic plane-stress condition given by Eq. (62). Further details on this iterative procedure can be found in [18].

4. Numerical results and discussions

4.1. Material data

The following choices for materials and parameters are adopted in the subsequent simulations both at the single crystal and polycrystal scales:

- elasticity is assumed to be linear and isotropic. The Young modulus and the Poisson ratio are taken to be equal to 210 GPa and 0.3, respectively;
- the initial critical shear stress τ_0 is assumed to be the same for all slip systems, and it is taken to be equal to 40 MPa;
- hardening is assumed to be isotropic. Accordingly, the different components of the hardening matrix $\mathbf{h}$ are assumed to be the same and equal to h. The hardening variable h is defined by the following power-type law:

$$h = h_0 \left(1 + \frac{h_0 \Gamma}{\tau_0 n}\right)^{\mathrm{n}-1} ; \qquad \Gamma = \sum_{\alpha=1}^{6} (\gamma^{\alpha} + \gamma^{\alpha+6}) \tag{63}$$

where h_0 and n are two hardening parameters set to 390 MPa and 0.35, respectively.

4.2. Single-crystal simulations

The main objective of this section is to demonstrate that the planar single crystal model leads to the same numerical predictions as the three-dimensional one, when the loading is applied under plane-stress conditions. To this aim, two bi-dimensional loading paths are applied to the plane single-crystal model and the three-dimensional one, respectively. These loading paths are defined by the following microscopic velocity gradients:

$$\mathbf{g} = \begin{bmatrix} 1 & 0 \\ 0 & -1/2 \end{bmatrix}; \qquad \mathbf{g}_{3\mathcal{D}} = \begin{bmatrix} 1 & 0 & 0 \\ 0 & -1/2 & 0 \\ 0 & 0 & ? \end{bmatrix} \tag{64}$$

For the three-dimensional single-crystal model, the component $g_{3\mathcal{D}33}$ is a priori unknown, and it is determined by an iterative procedure so that the plane-stress condition is satisfied:

$$\dot{\sigma}_{3\mathcal{D}33} = 0 \tag{65}$$

For these two types of numerical simulations, the initial value of the angle φ describing the rotation of the intermediate configuration of the single crystal with respect to the current one (see Eq. (16)) is set to $\pi/3$.

Fig. 3 compares the predictions obtained by the two single-crystal models in terms of the evolution of the slip of crystallographic slip systems. Eight (resp. four) slip systems are activated when the three-dimensional (resp. two-dimensional) single crystal model is used. By examining the correspondence between the two models, in terms of the crystallographic slip systems detailed in Table 2, and by analyzing the curves of Fig. 3, one can conclude that the two models lead to the

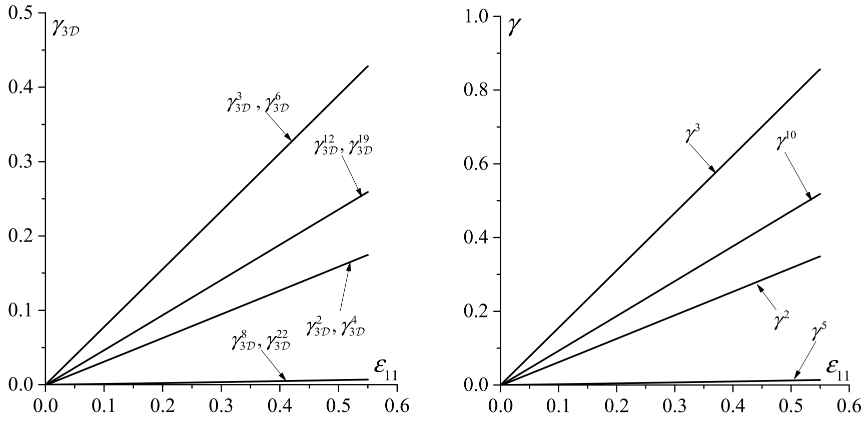

(a) (b)

Fig. 3. Evolution of the slip of the active slip systems: (a) three-dimensional single-crystal model; (b) two-dimensional single-crystal model.

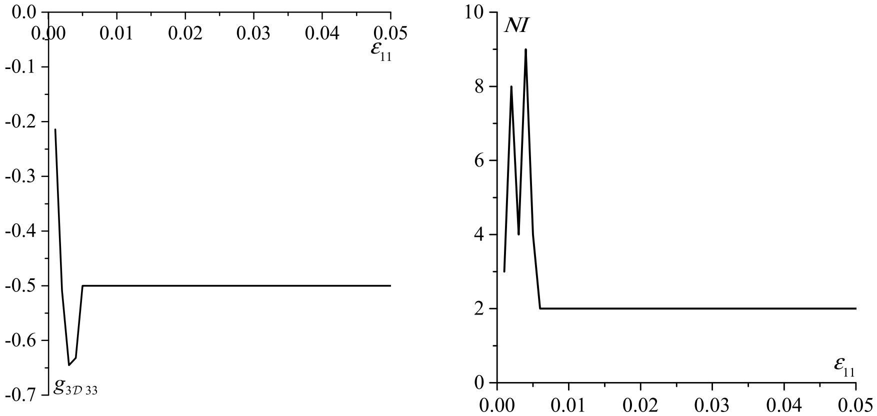

(a) (b)

Fig. 4. Enforcement of the plane-stress condition for the three-dimensional model: (a) evolution of the unknown component $g_{3\mathcal{D}33}$; (b) evolution of the number of iterations required to enforce Eq. (65).

same mechanical response. For instance, in the three-dimensional model, systems 3 and 6 are active with the same evolution of slip amplitude during loading. On the other hand, in the two-dimensional model, slip system 3 is active with a slip amplitude equal to the sum of the slip amplitude of systems 3 and 6 in the three-dimensional model. The slip evolution of the other active slip systems can be analyzed in a similar way ($\gamma^{10} = \gamma_{3\mathcal{D}}^{12} + \gamma_{3\mathcal{D}}^{19}$; $\gamma^{2} = \gamma_{3\mathcal{D}}^{2} + \gamma_{3\mathcal{D}}^{4}$ and $\gamma^{5} = \gamma_{3\mathcal{D}}^{8} + \gamma_{3\mathcal{D}}^{22}$). Considering the above-described constitutive equations, one can conclude that the similarity in the evolution of slip of the crystallographic systems leads to a perfect similarity in the evolution of the other mechanical variables (stress tensor, critical shear stresses, plastic deformation, crystallographic orientation). This result is quite expected and confirms the idea that both single crystal models lead to the same prediction when a biaxial loading is applied under plane-stress conditions and with planar crystallographic orientation. Note that, by applying other types of biaxial loading and planar crystallographic orientations, the same trends and conclusions have been observed.

As previously explained, when the three-dimensional single-crystal model is considered, an iterative procedure is required to enforce the plane-stress condition expressed by Eq. (65). The need for such an iterative procedure is naturally avoided in the case of the two-dimensional single crystal model. The evolution of the unknown component $g_{3\mathcal{D}33}$ is shown in Fig. 4a. This component evolves rapidly at the beginning of loading (when the amount of plastic deformation is not yet dominant compared to the elastic counterpart), and tends to $-(g_{3\mathcal{D}11} + g_{3\mathcal{D}22})$ when the deformation becomes important. This result is expectable considering the incompressibility of plastic deformation. The evolution of the number of iterations (denoted NI) required to enforce the plane-stress condition is shown in Fig. 4b. This number varies between 9 (at the beginning of loading, when the elastic strain is not very small compared to the plastic strain) and 2. It must be noted that this number is strongly dependent on the size of the time increment Δt, which is set to 0.001 s in the current simulations.

The comparison of the CPU times required by the two different single crystal models for the above simulations reveals that the two-dimensional model is significantly more efficient than the three-dimensional one. Indeed, 4 s are required for the simulations with the two-dimensional model, versus 11 s for the three-dimensional one. This large difference is expectable and can be explained by the size of the mathematical system in Eq. (47) to be solved to compute the slip rates. This

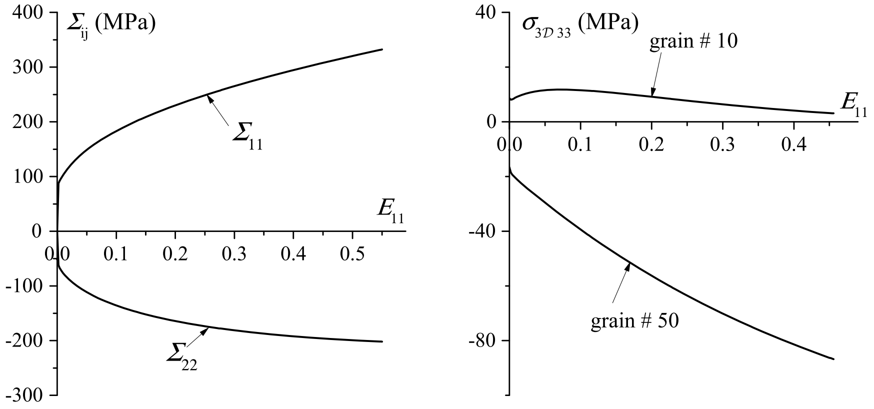

(a) (b)

Fig. 5. (a) Effect of the polycrystal model on the evolution of the macroscopic stress components Σ_{11} and Σ_{22} as functions of E_{11}; (b) evolution of the microscopic stress component $\sigma_{3\mathcal{D}33}$ as a function of E_{11} for two arbitrarily selected single crystals.

size is proportional to the number of potentially active slip systems. Furthermore, the application of the iterative algorithm to ensure the plane-stress condition in the case of the three-dimensional model considerably increases the computation time. Consequently, from the results reported in Figs. 3 and 4, and the comparison of the CPU times, one can conclude that the two-dimensional single-crystal model is much more suitable than the three-dimensional one for the simulation of the mechanical behavior of single crystals submitted to biaxial loading under a plane-stress state.

4.3. Polycrystal simulations

This section is focused on the investigation of the effect of the single-crystal model on the numerical predictions at the polycrystalline scale. To this end, we consider a polycrystalline aggregate composed of 1000 grains, which have the same initial volume fraction. The initial crystallographic texture associated with this aggregate is assumed to be isotropic, and the initial orientation $\varphi_0(i)$ corresponding to the ith grain (with $1 \leq i \leq 1000$) is set to $\varphi_0(i) = (180(i-1))/1000$.

As for the case of the single crystal, the predictions obtained with the three-dimensional polycrystal model are compared to those given by the two-dimensional model. The loading paths adopted in these comparisons are defined by the following macroscopic velocity gradients:

$$\mathbf{G} = \begin{pmatrix} 1 & 0 \\ 0 & -1/2 \end{pmatrix}; \qquad \mathbf{G}_{3\mathcal{D}} = \begin{pmatrix} 1 & 0 & 0 \\ 0 & -1/2 & 0 \\ 0 & 0 & ? \end{pmatrix} \tag{66}$$

The unknown component $G_{3\mathcal{D}33}$ is taken to be the same for all the single crystals (since the Taylor multiscale scheme is used), and it is determined by the enforcement of the macroscopic plane-stress condition ($\Sigma_{3\mathcal{D}33} = 0$).

The evolutions of the macroscopic stress components Σ_{11} and Σ_{22} as functions of the macroscopic strain component E_{11} are plotted in Fig. 5a. In this figure, both results obtained with the two-dimensional and three-dimensional models are presented. However, due to the perfect similarity of the results yielded by the two models, the curves plotted are indistinguishable. Despite the perfect agreement in the evolution of the macroscopic stress components, as predicted by both polycrystal models, the results at the microscopic scale are different. Indeed, as demonstrated in Fig. 5b, the microscopic normal stress $\sigma_{3\mathcal{D}33}$ is different from zero for grains #10 and #50 (but the magnitude of this normal stress component remains small compared to the magnitude of the macroscopic stress components Σ_{11} and Σ_{22}). These results reveal that the microscopic plane-stress condition is not fulfilled for these grains. Note that these grains have been chosen arbitrarily to illustrate this observation. More generally, this non-satisfaction of the microscopic plane-stress condition is a common trend for all the grains that compose the polycrystalline aggregate. This observation motivates the choice of the planar polycrystal model, instead of the three-dimensional one, to study the ductility of very thin sheet metals under biaxial loading. Indeed, the number of grains through the thickness for very thin sheets does not exceed 5, and the plane-stress condition should be obviously verified in all the grains that compose the polycrystalline aggregate.

Attention is directed now towards the analysis of the effect of the polycrystal model on the localization bifurcation predictions. It is now widely recognized that the incremental tangent modulus $\mathbf{L}$ plays a major role in the determination of the limit strains in the framework of bifurcation theory. Therefore, before analyzing the effect of the polycrystalline model (two-dimensional or three-dimensional) on the prediction of plastic flow localization, let us first examine the effect of the constitutive modeling on the evolution of the components of this tangent modulus. To this end, the evolution of the components L_{1111}, L_{2222}, L_{1122} and L_{1212} as a function of the macroscopic strain component E_{11} is plotted in Fig. 6 for three representative strain–path ratios ($\rho = -0.5, \rho = -0.2,$ and $\rho = 0$). It can be first observed that the evolutions

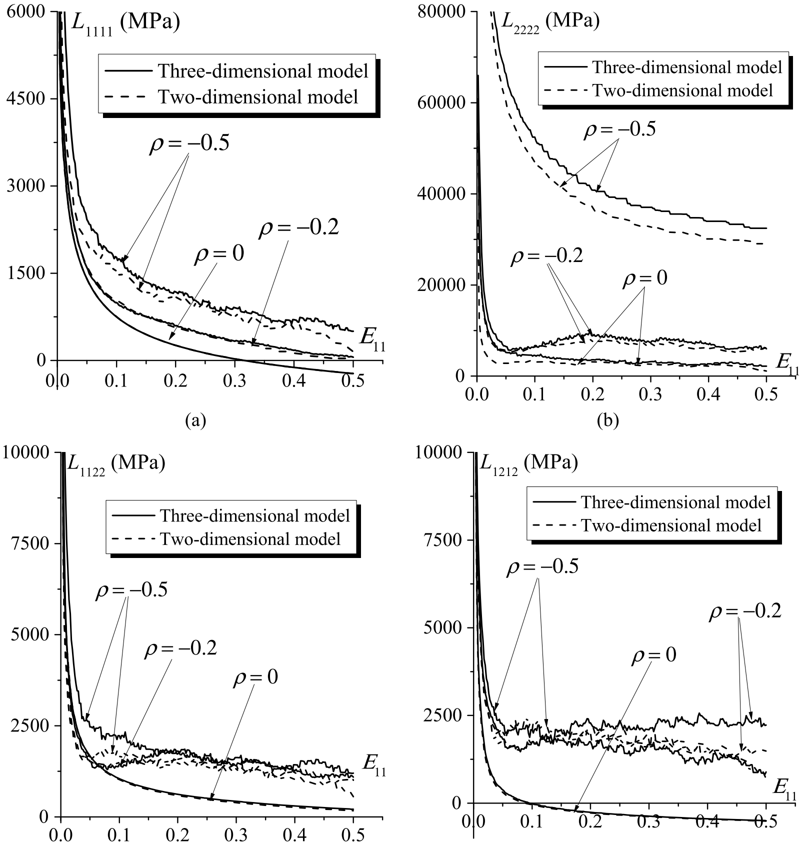

(a) (b)

(c) (d)

Fig. 6. Evolution of some components of the macroscopic tangent modulus as a function of E_{11} for three different strain–path ratios ($\rho = -0.5$, $\rho = -0.2$, and $\rho = 0$): (a) evolution of L_{1111}; (b) evolution of L_{2222}; (c) evolution of L_{1122}; (d) evolution of L_{1212}.

of these tangent modulus components, as predicted by both polycrystal models (two-dimensional or three-dimensional), are only very slightly different, especially for the strain–path ratios $\rho = -0.2$ and $\rho = 0$. This means that the microscopic plane-stress condition, which seems to be the main difference between the two polycrystalline models, has a small effect on the evolution of the macroscopic tangent modulus. For the case of uniaxial tensile strain path ($\rho = -0.5$), the evolution of the different components of the macroscopic tangent modulus is not quite smooth. This is very likely attributable to the significant effect of the crystallographic texture for this strain path, on the one hand, and to the fact that the description of plastic accommodation is lacking in the Taylor model, on the other hand. Indeed, within this full-constraints scale-transition scheme, each grain deforms independently of the other grains, and the interaction with the neighbors is not accounted for. For the different models and strain paths, the magnitude of components L_{1111}, L_{2222} and L_{1122} is reduced, after the preliminary stage of elastic deformation, to reach sometimes very low values. It is especially noticed that the shearing component L_{1212} is significantly reduced during the deformation and becomes very low (and sometimes even negative) compared to the other components. This result is a natural outcome of the multi-slip character of crystal plasticity, which leads to the formation of vertices at the current points of the Schmid yield surfaces of single crystals (see Fig. 1). The reduction of these shearing components is the main destabilizing factor responsible for bifurcation, thus promoting early plastic strain localization.

The evolution of the minimum of the determinant of the acoustic tensor, over all possible band orientations, as a function of the major strain E_{11} is reported in Fig. 7. The results of this figure confirm the trends observed in Fig. 6, namely the similarity between the predictions obtained by the two polycrystalline models. As previously stated, localized necking is detected when the determinant of the acoustic tensor reaches zero.

To assess the efficiency of each polycrystalline model, a comparative study is reported in Fig. 8, with regard to the CPU time required for the prediction of localized necking for the three strain paths studied in Fig. 7. As expected, the CPU time decreases when the strain–path ratio increases for both polycrystal models. This result may be explained by the decrease of the limit strain with the strain–path ratio, as observed in Fig. 7. Furthermore, the planar polycrystal model appears to be significantly more efficient than the three-dimensional model in terms of CPU time. This observation is in accordance with the comparison conducted at the single crystal scale, and can be explained by the same reasons given previously: the number of potentially active slip systems determined by the three-dimensional model, which is the double of its counterpart

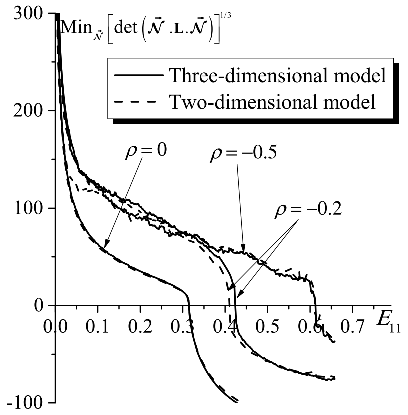

Fig. 7. Evolution of the minimum of the determinant of the acoustic tensor, as a function of E_{11}, for three representative strain–path ratios ($\rho = -0.5$, $\rho = -0.2$, and $\rho = 0$).

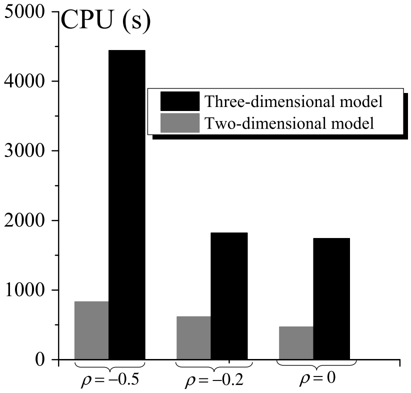

Fig. 8. Comparison of the efficiency of the two polycrystalline models: CPU time corresponding to the prediction of strain localization for three representative strain–path ratios ($\rho = -0.5$, $\rho = -0.2$, and $\rho = 0$).

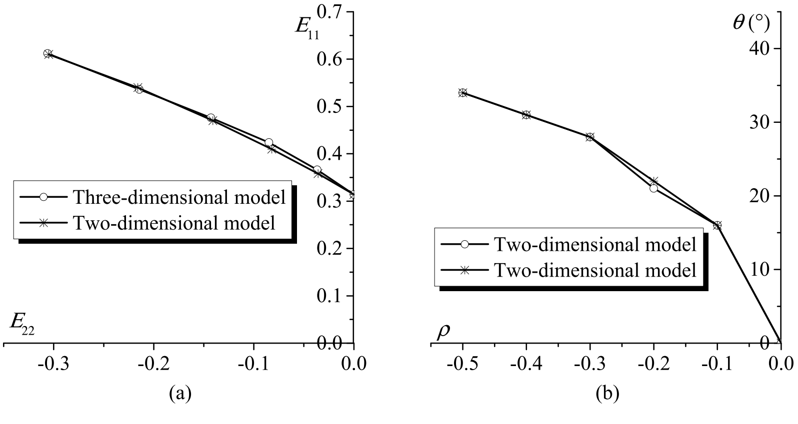

Fig. 9. FLDs and necking band orientations, as predicted by the two-dimensional and three-dimensional polycrystalline models: (a) FLDs; (b) necking band orientation for different strain paths.

determined by the two-dimensional model, and the macroscopic plane-stress condition, which is naturally fulfilled with the two-dimensional model and which needs to be enforced by an iterative computation when the three-dimensional model is used. The results of Fig. 7 and Fig. 8 highlight the much better performance of the planar model, compared to the three-dimensional one, in the prediction of localized necking in very thin sheets using multiscale schemes.

The effect of the polycrystalline model on the prediction of forming limit diagrams and necking band orientations is studied in Fig. 9. Note that the curves reported in Fig. 9a and 9b are almost indistinguishable. These results generalize the previous observations regarding the consistency and similarity of the predictions yielded by the two polycrystalline models, and confirm once again the superiority of the two-dimensional model compared to the three-dimensional one.

5. Conclusions

In the present investigation, a powerful numerical tool, specifically designed for the prediction of localized necking in very thin sheet metals, has been developed. The proposed tool is based on the coupling between the full-constraints Taylor scale-transition model and bifurcation theory. Biaxial loading paths have been applied under plane-stress conditions to predict the occurrence of strain localization. Consequently, a two-dimensional model has been advantageously developed to describe the mechanical behavior at the single-crystal scale. Relevant aspects of the numerical integration of this single-crystal model have been discussed, and particular attention has been devoted to the efficient and accurate computation of the slip rates of the crystallographic slip systems. The numerical simulations reveal that this planar crystal plasticity model is much more suitable than the three-dimensional one for the prediction of localized necking in thin metal sheets. Indeed, the two-dimensional model allows us to obtain almost the same results as the three-dimensional model, while significantly reducing the CPU time. Furthermore, the use of the two-dimensional model allows us to rigorously ensure the plane-stress state at both the single crystal and polycrystal scales.

The current study will be extended in future investigations to other multiscale schemes, which are more sophisticated than the Taylor model, such as the self-consistent approach [28] and the periodic homogenization technique [47].

References

[1] H. Badreddine, C. Labergère, K. Saanouni, Ductile damage prediction in sheet and bulk metal forming, C. R. Mecanique 344 (2016) 296–318.
[2] H. Badreddine, K. Saanouni, A. Dogui, On non-associative anisotropic finite plasticity fully coupled with isotropic ductile damage for metal forming, Int. J. Plast. 26 (2010) 1541–1575.
[3] K. Saanouni, Damage Mechanics in Metal Forming, ISTE/Wiley, London, ISBN 978-1-84821-3487, 2012.
[4] A. Abdul-Latif, K. Saanouni, Damaged anelastic behavior of FCC polycrystalline metals with micromechanical approach, Int. J. Damage Mech. 3 (1994) 237–259.
[5] M. Boudifa, K. Saanouni, J.-L. Chaboche, A micromechanical model for inelastic ductile damage prediction in polycrystalline metals for metal forming, Int. J. Mech. Sci. 51 (2009) 453–464.
[6] S.P. Keeler, W.A. Backofen, Plastic instability and fracture in sheets stretched over rigid punches, ASM Trans. Q. 56 (1963) 25–48.
[7] K.W. Neale, E. Chater, Limit strain predictions for strain-rate sensitive anisotropic sheets, Int. J. Mech. Sci. 22 (1980) 563–574.
[8] M. Kuroda, V. Tvergaard, Forming limit diagrams for anisotropic metal sheets with different yield criteria, Int. J. Solids Struct. 37 (2000) 5037–5059.
[9] J.W. Hutchinson, K.W. Neale, Sheet necking-III. Strain-rate effects, in: D.P. Koistinen, N.M. Wang (Eds.), Mechanics of Sheet Metal Forming, Plenum Press, New York, London, 1978, pp. 269–285.
[10] M. Ben Bettaieb, F. Abed-Meraim, Strain rate effects on the enhancement of localized necking in substrate-supported metal layers, Int. J. Adv. Manuf. Technol. 92 (2017) 3461–3480.
[11] L.Z. Mansouri, H. Chalal, F. Abed-Meraim, Ductility limit prediction using a GTN damage model coupled with localization bifurcation analysis, Mech. Mater. 76 (2014) 64–92.
[12] H. Chalal, F. Abed-Meraim, Hardening effects on strain localization predictions in porous ductile materials using the bifurcation approach, Mech. Mater. 91 (2015) 152–166.
[13] K. Inal, K.W. Neale, A. Aboutajeddine, Forming limit comparisons for FCC and BCC sheets, Int. J. Plast. 21 (2005) 1255–1266.
[14] Z. Marciniak, K. Kuczynski, Limit strains in processes of stretch-forming sheet metal, Int. J. Mech. Sci. 9 (1967) 609–620.
[15] J.W. Signorelli, M.A. Bertinetti, P.A. Turner, Predictions of forming limit diagrams using a rate-dependent polycrystal self-consistent plasticity model, Int. J. Plast. 25 (2009) 1–25.
[16] C. Schwindt, F. Schlosser, M.A. Bertinetti, J.W. Signorelli, Experimental and visco-plastic self-consistent evaluation of forming limit diagrams for anisotropic sheet metals: an efficient and robust implementation of the M–K model, Int. J. Plast. 73 (2015) 62–99.
[17] R. Knockaert, Y. Chastel, E. Massoni, Forming limits predictions using rate-independent polycrystalline plasticity, Int. J. Plast. 18 (2002) 231–247.
[18] H.K. Akpama, M. Ben Bettaieb, F. Abed-Meraim, Localized necking predictions based on rate-independent self-consistent polycrystal plasticity: bifurcation analysis versus imperfection approach, Int. J. Plast. 91 (2017) 205–237.
[19] G. Franz, F. Abed-Meraim, M. Berveiller, Strain localization analysis for single crystals and polycrystals: towards microstructure-ductility linkage, Int. J. Plast. 48 (2013) 1–33.
[20] S. Stören, J.R. Rice, Localized necking in thin sheets, J. Mech. Phys. Solids 23 (1975) 421–441.
[21] K. Yoshida, M. Kuroda, Comparison of bifurcation and imperfection analyses of localized necking in rate-independent polycrystalline sheets, Int. J. Solids Struct. 49 (2012) 2073–2084.
[22] Y. Tadano, K. Yoshida, M. Kuroda, Plastic flow localization analysis of heterogeneous materials using homogenization-based finite element method, Int. J. Mech. Sci. 72 (2013) 63–74.
[23] E. Schmid, W. Boas, Plasticity of Crystals, Chapman and Hall, London, 1935.
[24] A. Chenaoui, F. Sidoroff, A. Hihi, The texture evolution of a planar polycrystal, J. Mech. Phys. Solids 48 (2000) 2559–2584.
[25] J.W. Hutchinson, K.W. Neale, A. Needleman, Sheet necking-I. Validity of plane stress assumptions of the long-wavelength approximation, in: D.P. Koistinen, N.M. Wang (Eds.), Mechanics of Sheet Metal Forming, Plenum, 1978, pp. 111–126.
[26] R.J. Asaro, J.R. Rice, Strain localization in ductile single crystals, J. Mech. Phys. Solids 25 (1977) 309–388.
[27] R.J. Asaro, Geometrical effects in the homogeneous deformation of ductile single crystals, Acta Metall. 27 (1979) 445–453.
[28] T. Iwakuma, S. Nemat-Nasser, Finite elastic–plastic deformation of polycrystalline metals, Proc. R. Soc. Lond. Ser. A, Math. Phys. Sci. 394 (1984) 87–119.
[29] J.R. Rice, The localization of plastic deformation, in: 14th International Congress of Theoretical and Applied Mechanics, 1976, pp. 207–220.
[30] Y.F. Dafalias, Planar double-slip micromechanical model for polycrystal plasticity, J. Eng. Mech. 119 (1993) 1260–1284.
[31] A. Kumar, P.R. Dawson, The simulation of texture evolution with finite elements over orientation space II. Application to planar crystals, Comput. Methods Appl. Mech. Eng. 130 (1996) 247–261.
[32] M.M. Rashid, Texture evolution and plastic response of two-dimensional polycrystals, J. Mech. Phys. Solids 40 (1992) 1009–1029.
[33] V.C. Prantil, J.T. Jenkins, P.R. Dawson, An analysis of texture and plastic spin for planar polycrystals, J. Mech. Phys. Solids 41 (1993) 1357–1382.
[34] A.H. Shalaby, K.S. Havner, A general kinematical analysis of double slip, J. Mech. Phys. Solids 26 (1978) 79–92.

[35] J. Boukadia, F. Sidoroff, Simple shear and torsion of a perfectly plastic single crystal in finite transformation, Arch. Mech. 40 (1988) 497–513.
[36] J. Boukadia, A. Chenaoui, F. Sidoroff, Simple shear in FCC single crystals at large deformations, in: C. Teodosiu, J.-L. Raphanel, F. Sidoroff (Eds.), Large Plastic Deformation, Proc. Int. Sem. MECAMAT, Fontainebleau, France, 1991, pp. 109–116.
[37] J. Mandel, Généralisation de la théorie de la plasticité de W.T. Koiter, Int. J. Solids Struct. 1 (1965) 273–295.
[38] R. Hill, J.R. Rice, Constitutive analysis of elastic–plastic crystals at arbitrary strain, J. Mech. Phys. Solids 20 (1972) 401–413.
[39] R.J. Asaro, Crystal plasticity, J. Appl. Mech. 50 (1983) 921–934.
[40] R. Hill, Generalized constitutive relations for incremental deformation of metal crystals by multislip, J. Mech. Phys. Solids 14 (1966) 95–102.
[41] R.I. Borja, J.R. Wren, Discrete micromechanics of elastoplastic crystals, Int. J. Numer. Methods Eng. 36 (1993) 3815–3840.
[42] M. Ben Bettaieb, O. Débordes, A. Dogui, L. Duchêne, C. Keller, On the numerical integration of rate independent single crystal behavior at large strain, Int. J. Plast. 32–33 (2012) 184–217.
[43] H.K. Akpama, M. Ben Bettaieb, F. Abed-Meraim, Numerical integration of rate-independent BCC single crystal plasticity models: comparative study of two classes of numerical algorithms, Int. J. Numer. Methods Eng. 108 (2016) 363–422.
[44] L. Anand, M. Kothari, A computational procedure for rate-independent crystal plasticity, J. Mech. Phys. Solids 44 (1996) 525–558.
[45] A. Fischer, A special Newton-type optimization method, Optimization 24 (1992) 269–284.
[46] A. Fischer, Solution of monotone complementarity problems with locally Lipschitzian functions, Math. Program. 76 (1997) 513–532.
[47] S. Elbououni, S. Bourgeois, O. Débordes, A. Dogui, Simulation by periodic homogenization of the behavior of a polycrystalline material in large elasto-plastic transformations, J. Phys. IV 105 (2003) 123–130.